Ring charging of a single silicon dangling bond imaged by noncontact atomic force microscopy

Natalia Turek, S. Godey, D. Deresmes, Thierry Melin

Ring charging of a single silicon dangling bond imaged by noncontact atomic force microscopy

Natalia Turek, Sylvie Godey, Dominique Deresmes, and Thierry Mélin*

Univ. Lille, CNRS, Centrale Lille, Junia, Univ. Polytechnique Hauts-de-France, UMR 8520 - IEMN - Institut d'Electronique de Microélectronique et de Nanotechnologie, F-59000 Lille, France

(Received 25 May 2020; accepted 9 December 2020; published 29 December 2020)

The electrostatic properties of defects of the Si(111)-$(\sqrt{3}\times\sqrt{3})R^{\circ}30$ surface are studied using noncontact atomic force microscopy and Kelvin probe force microscopy with subnanometer resolution and subelementary charge sensitivity. We identify nonparabolicities in the frequency-voltage spectroscopy of single dangling bonds (DBs), which reveal the transition from empty to single electronically occupied DBs. Kelvin probe imaging reveals that the DB charging, however, occurs with a ring shape with radius ∼500 pm located along the circumference of the DB wave function. The ring charging is explained by a tip-induced modulation of the hole recombination rate at the DB-substrate interface.

DOI: 10.1103/PhysRevB.102.235433

I. INTRODUCTION

Noncontact atomic force microscopy (nc-AFM) and Kelvin probe force microscopy (KFPM) with atomic or submolecular resolution have for the last decade enabled important advances in mapping the structure [1] and electrostatic properties of surfaces, adatoms, and molecules [2–7]. While most studies have been conducted on metal substrates, semiconductors offer large perspectives in terms of confined electronic systems, e.g., quantum dots [8,9]. An ultimate confined system is a surface adatom dangling bond (DB) consisting of a single electronic state in the bandgap of a semiconductor, whose charging can be controlled by a scanning-probe microscope [10,11]. DBs have been proposed for binary logic [12] and data storage [13,14] applications. They reveal a rich fundamental physics, such as polaronic transport [15,16] and carrier dynamics [17,18].

Here, we image silicon DBs from an electrostatic point of view using KPFM techniques. We work on a *p*-doped Si(111) surface, using the Si(111)-$(\sqrt{3}\times\sqrt{3})R^{\circ}30$ surface reconstruction. The ability to produce *images* of elementary charge features with subnanometer resolution is first demonstrated using buried ionized dopants, surface vacancies, and the DB empty state, which carry, respectively, $-e$, $0e$, and $+e$ charges. Nonparabolicity effects are then identified in the frequency-voltage spectroscopy of single DBs and are attributed to the transition between the empty and the first occupied DB states. KPFM imaging reveals that the DB charging remarkably occurs with a ring shape localized at the periphery of the DB wave function, which is explained by a tip-induced modulation of the carrier recombination rate at the DB-substrate interface. Unveiling such a modulation or gating effect at the subnanometer scale from KPFM mapping illustrates the possibility of gaining new insights into the physics of ultimate confined semiconductor systems using highly resolved nc-AFM techniques, compared to previous scanning tunneling microscopy studies [19]. It also demonstrates the need for future microsopic theories of such phenomena.

II. EXPERIMENTAL DETAILS

Experiments have been carried out at $T = 4$ K using a Joule-Thomson STM/AFM (SPECS, Berlin) with a base pressure of 10^{-10} mbar. The samples consist of *p*-type Si(111)

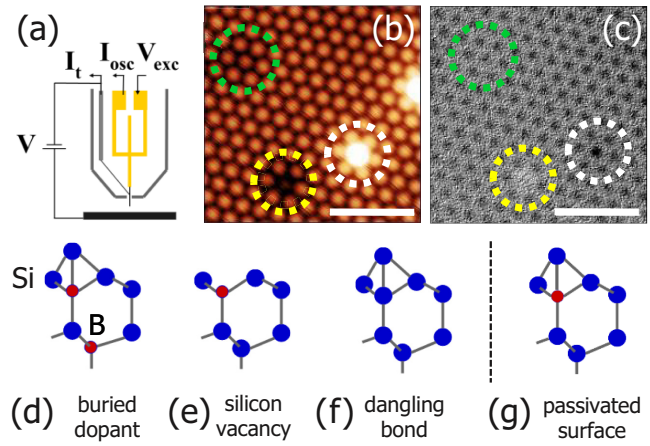

FIG. 1. (a) Length-extensional resonator sensor (yellow) used for STM and nc-AFM. V is the voltage applied to the sample; I_t, the tunnel current. The oscillator is excited using a bias V_{exc} on the quartz, and the oscillation at the frequency $f_0 + \Delta f$ is tracked from the current I_{osc}. (b) Empty-state STM image ($V = +1.5$ V, $I_t = 10$ pA, 160-pm color z range, 3-nm scale bar) of the Si(111)-$(\sqrt{3}\times\sqrt{3})R^{\circ}30$ reconstruction. The highlighted defects are a buried dopant (green), a silicon vacancy (yellow), and a silicon DB (white). (c) Corresponding atomic-resolution nc-AFM open-loop frequency shift image (0.3-Hz Δf grayscale), using $A_{pp} = 100$ pm. (d–f) Defect structures: buried dopant, vacancy, and DB. (g) Passivated surface adatom of the Si(111)-$(\sqrt{3}\times\sqrt{3})R^{\circ}30$ reconstruction, corresponding to all atoms visible in (b) and (c) except defects.

*thierry.melin@iemn.fr

degenerately doped with boron (resistivity of ≈1 mΩ · cm at 300 K), prepared by thermal annealing up to 1200°C to obtain a Si(111)-($\sqrt{3} \times \sqrt{3}$)R°30 surface reconstruction (see Refs. [10,13,16,20]) for the surface preparation and defect identification). They have been investigated by scanning tunneling microscopy (STM) and nc-AFM, using length-extensional resonators with W tips (Kolibri sensors; SPECS, Berlin) of oscillation frequency $f_0 \approx 1$ MHz and quality factor $Q \approx 10^5$ [21,22]. The tips have been prepared by Ar sputtering and substrate conditioning [20,23]. The resonator excitation is generated by a bias V_{exc} applied to the quartz sensor [Fig. 1(a)] at a frequency close to f_0, and the tip oscillation is monitored via the I_{osc} current. We used the peak-to-peak oscillation amplitude $A_{pp} = 100$ pm for nc-AFM. The oscillation frequency shift Δf is determined from the I_{osc} by a phase-locked loop electronics (Nanonis; SPECS, Zürich). The tunneling current I_t flowing through the grounded tip (with the sample biased at a voltage V) is collected by a separate electrode. nc-AFM is obtained after a preliminary STM scan, by passing the tip parallel to the substrate plane and recording Δf for $V = 0$. KPFM consists of recording $\Delta f(V)$ local spectroscopies over a predefined grid (data acquisition of a few hours), with the tip retracted by 150 pm from nc-AFM conditions, and using $A_{pp} = 200$ pm for noise issues.

III. nc-AFM AND KPFM IMAGING OF SINGLE IONIZED BURIED DOPANTS

Figure 1(b) shows an empty-state STM image of the surface, with three defects: a subsurface ionized boron dopant [Fig. 1(d)], a surface silicon adatom vacancy [Fig. 1(e)], and an unpassivated surface Si adatom leading to a DB [Fig. 1(f)], highlighted by green, yellow, and white dashed circles, respectively. The defects are also observed in the atomic resolution nc-AFM image in Fig. 1(c) [20] (frequency shift image acquired with z feedback loop off).

We use KPFM to image the electrostatics of these defects, starting with the buried boron dopant. A control filled-state STM image is shown in Fig. 2(a), together with the 15 × 15 grid used in the spectroscopy experiment. The in-plane drift (here <100 pm/h) is systematically verified. We checked that the $\Delta f(V)$ [example in Fig. 2(b)] spectroscopies are hysteresis free. They are analyzed through a quadratic fit, $A + B \times (V - V_s)^2$, to experimental data, using the method of least squares. A is the resonator frequency shift for $V = V_s$ and accounts for van der Waals, repulsive forces and image charge effects, but also includes a residual offset on the determination of f_0; B accounts for the tip-surface capacitance second derivative; and V_s is the local surface potential, including electrostatic (i.e., charging) effects. The reconstructed image of V_s constitutes the KPFM image. Since V is applied to the sample, a positive (negative) surface charge will be compensated by a negative (positive) surface potential contribution, leading to a dark (bright) feature in the KPFM image. The error on V_s is defined on each grid point as the sample voltage offset required to increase the residue of the quadratic fit to $\Delta f(V)$ by a factor of 2, while keeping A and B constant.

Grid maps of A and B for the buried dopant in Fig. 2(a) are shown in Figs. 2(c) and 2(d). The faint observed evolution corresponds to a weak vertical drift of the tip. The error on V_s [Fig. 2(f)] evidences a KPFM accurary of the order of a few millivolts. The KPFM map [Fig. 2(e)] shows a highlighted bright feature of relative amplitude ≈40 mV and radius ≈1 nm. It corresponds to the negative potential expected for the ionized boron dopant ($-e$ charge). A similar experiment showed no detectable charge for the Si vacancy (Supplemental Material, Fig. S1 [24]). This demonstrates the ability of length-extensional resonators to map single charge features at subnanometer resolution, as expected theoretically [25] and originally achieved using tuning forks [2].

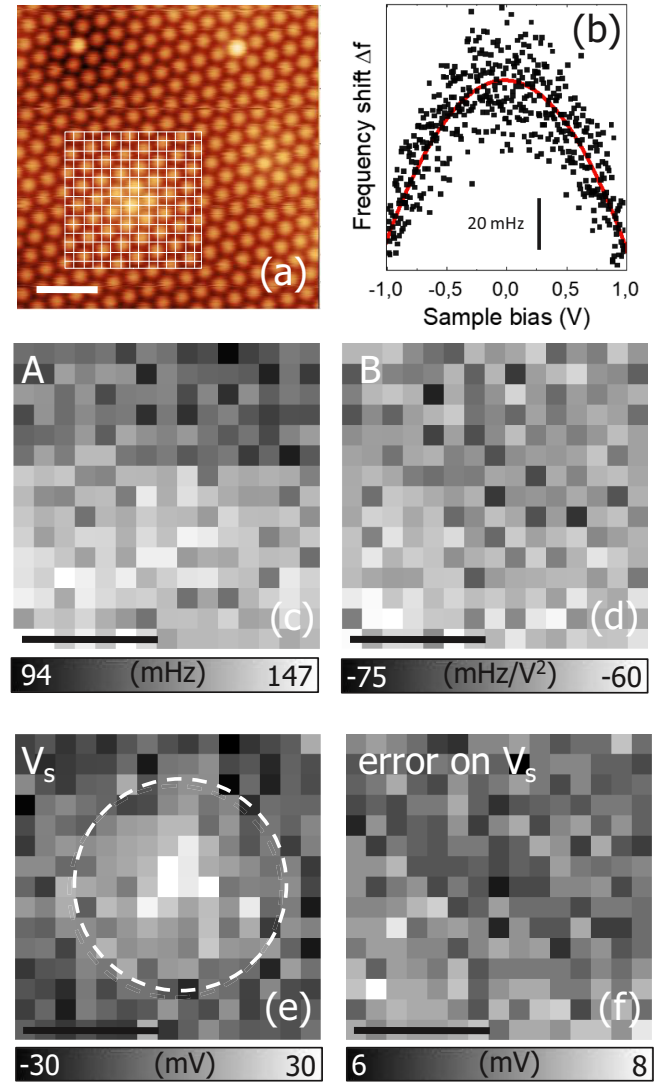

FIG. 2. (a) STM image ($V = -0.7$ V, $I_t = 10$ pA, 2-nm scale bar), together with the 15 × 15 grid used in $\Delta f(V)$ spectroscopy experiments over an identified buried dopant. (b) Example of a locally acquired $\Delta f(V)$ spectroscopy curve, together with a quadratic fit, $A + B \times (V - V_s)^2$. (c) Reconstructed 15 × 15 grid of the fitted A parameter (in Hz) over the buried dopant. (d) Grid of the fitted B parameter (in Hz/V^2). (e) Grid of fitted V_s values (KPFM map), showing a highlighted bright feature (negative potential). (f) Reconstructed grid of the fit error on V_s. Scale bars are 2 nm in (c)–(f).

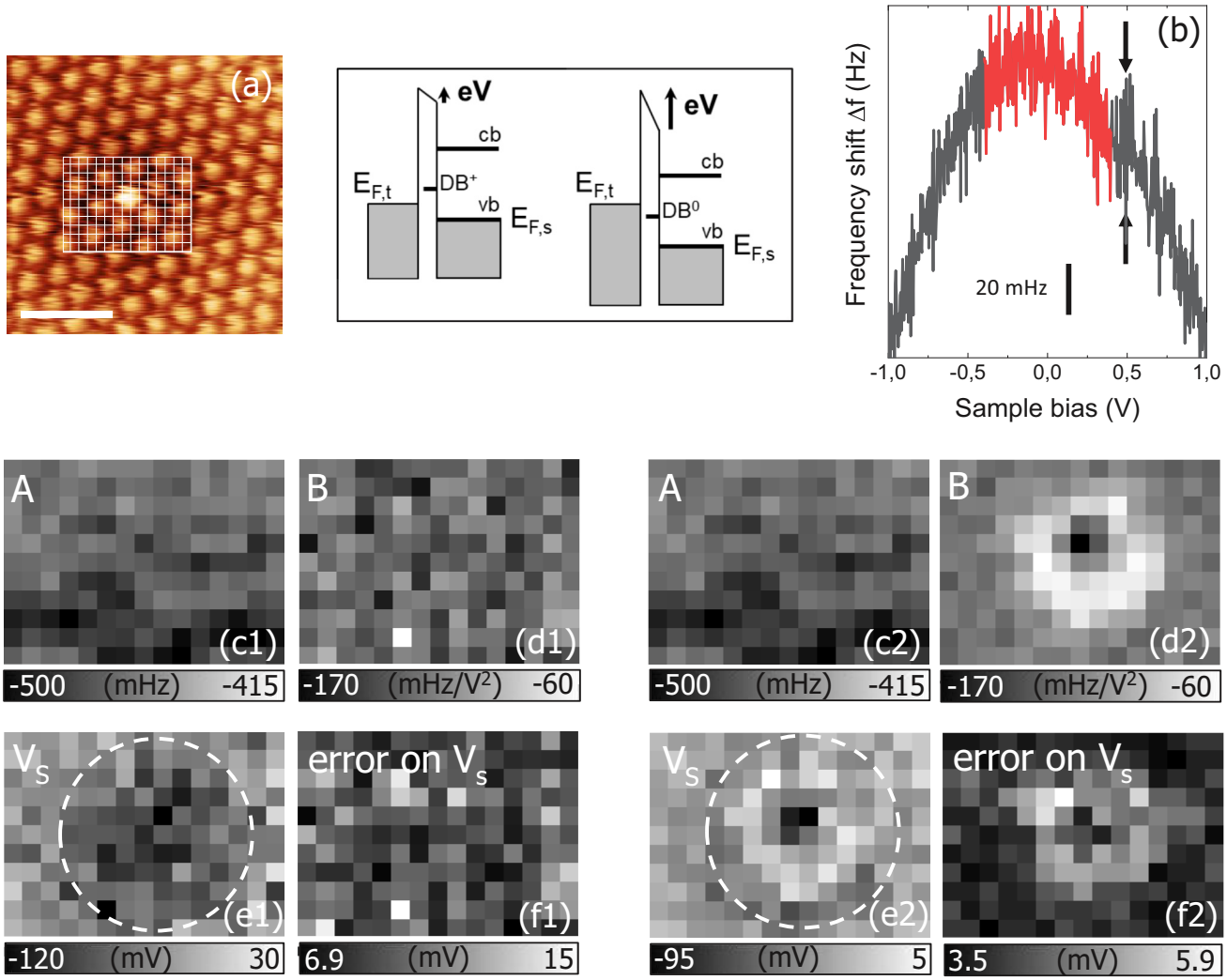

FIG. 3. (a) STM image (V = −0.7 V, I_t = 10 pA, 120-pm color scale, 2-nm scale bar) of a single dangling bond, with the 11 × 15 spectroscopy grid used in KPFM experiments. Inset: Energy diagrams of the tip-substrate junction with a bandgap DB state, in which $E_{F,t}$ and $E_{F,s}$ refer to the tip and substrate Fermi levels, and cb and vb to the substrate conduction and valence bands, respectively. Diagrams are shown at a low positive sample bias (left), in which the DB is in the unoccupied DB^+ state, and at a larger positive sample bias (right), for which the DB can be occupied by one electron in the neutral DB^0 state. (b) Example of a $\Delta f(V)$ spectroscopy showing a nonparabolicity effect (jump marked by arrows). The reduced voltage range in red [−0.4 V; +0.4 V] and the full range [−1 V; +1 V] have been used for the reconstructed grid images of the parameters A, B, and V_s and the error on V_s shown in (c1), (d1), (e1), and (f1) and in (c2), (d2), (e2), and (f2), respectively. The 11×15 grids in (c1)-(f1) and (c2)-(f2) correspond to image sizes of 2.05 nm × 2.8 nm.

IV. nc-AFM AND KPFM OF SINGLE SILICON DANGLING BONDS

We now focus on the Si DB, which constitutes the core of our paper. An STM image is given in Fig. 3(a) with the 11 × 15 KPFM grid. Schematic energy diagrams including the bandgap DB state are shown in the inset at small and large positive sample biases. The DB state is electronically unoccupied at a low voltage V and, thus, carries a charge $+e$ (DB^+ state). At a higher positive sample voltage, a current can flow through the DB, which can become populated by a single electron (neutral DB^0 state). The actual DB charge actually depends both on the electronic current and on the recombination rate with substrate holes. A DB charging by two electrons (DB^- state) can also be achieved [10] at a larger sample bias but is not investigated here. A similar behavior occurs for the DB on the H-Si(100) 2 × 1 surface [11].

We show in Fig. 3(b) a selected example of a $\Delta f(V)$ spectroscopy showing a nonparabolic feature marked by arrows, at a bias $V \simeq 0.5$ V. Its origin is discussed hereafter based on the DB charging. $\Delta f(V)$ data are first analyzed using a small voltage range [−0.4 V; 0.4 V] [data points in red in Fig. 3(b)], for which the DB is unoccupied. The grid images for A and B [Figs. 3(c1) and 3(d1)] reveal flat contributions, indicating a negligible drift. The image of V_s [Fig. 3(e1)] shows a dark feature (positive electrostatic potential), while the error on V_s [Fig. 3(f1)] remains featureless. The observation of a positive electrostatic potential is fully consistent with the DB^+ state expected for the DB at a low sample voltage (Fig. 3, inset). A further comparison of KPFM images for the buried dopant

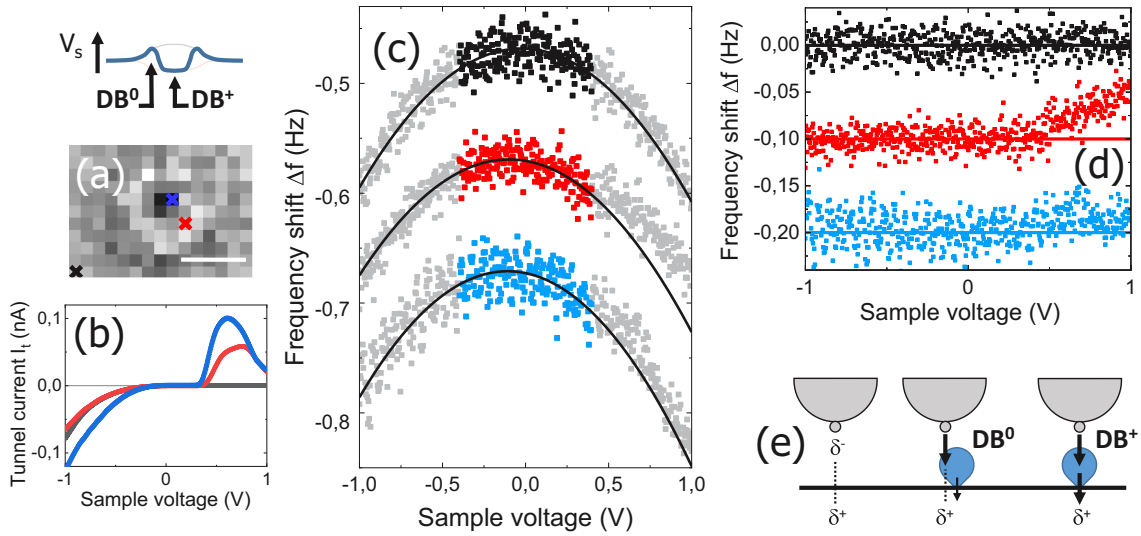

FIG. 4. (a) KPFM spectroscopy grid as in Fig. 3(e2) (1-nm scale bar) with a schematic cross section of the KPFM constrast. (b) $I_t(V)$ and (c) simultaneously recorded $\Delta f(V)$ spectroscopies acquired at the marked locations in (a). Colored points in $\Delta f(V)$ plots highlight the voltage range used for parabolic fits, which are shown as solid lines. (d) Difference between $\Delta f(V)$ and parabolic fits. (e) Model explaining the ring-shape charging as being due to a modulation of the hole recombination rate (see text).

($-e$ charge), silicon vacancy (neutral state), and DB^+ ($+e$ charge) is provided in the Supplemental Material, Fig. S2 [24].

To investigate the nonparabolicities, we reproduced the fitting procedure as in Figs. 3(c1)–3(f1), however, with a larger voltage range [−1 V; +1 V]. This analysis is purely phenomenological, since a quadratic model *does not* formally apply at a large positive bias. It, however, enables us to map where the nonparabolicities—and thus the charging effects—spatially occur. Indeed, a nonparabolicity in a $\Delta f(V)$ leads to fit deviations which impact both the fitted average curvature B and the surface V_s. DB fit results using a [−1 V; +1 V] voltage range are shown in Figs. 3(c2)–3(f2), as a comparison with images obtained in Figs. 3(c1)–3(f1). Nonparabolicities are observed with a ring shape of radius about 500 pm around the silicon DB, in both the V_s [Fig. 3(e2)] and the B [Fig. 3(d2)] images, which are correlated. They also appear in the error on V_s [Fig. 3(f2)], due to the unsatisfactory use of a quadratic model. The observation of a ring shape means that charging effects are lower at the location of the DB adatom but strikingly enhanced farther away from the adatom. The ring appears as a bright contrast in the KPFM (negative potential), which can be attributed to a local dipolar effect associated with the neutral DB^0 state (see Supplemental Material, Fig. S3 [24]).

We now analyze $\Delta f(V)$ spectroscopies over the substrate, charging ring, and DB adatom [black, red, and blue points in Fig. 4(a)]. Simultaneously recorded $I_t(V)$ tunnel spectroscopy data are shown in Fig. 4(b). The $I_t(V)$ spectroscopy over the substrate is typical of a p-type semiconductor. The Si(111)-$(\sqrt{3}\times\sqrt{3})R^\circ 30$ reconstruction, however, does not exhibit the degenerate character of the bulk Si substrate, as due to surface band bending. This indicates that the free hole density p at the sample surface is lower than the valence-band effective density of states at $T = 4$ K ($p < N_V \simeq 3\times10^{16}$ cm^{-3}). The $I_t(V)$ values acquired on the charging ring and DB adatom reveal the presence of the DB bandgap state, marked by the prominent peak at $V \approx 0.7$ V. The marked occurrence of a negative differential conductance is obtained for sub-nanoampere current levels because the tip is oscillated ($A_{pp} =$ 200 pm). The fact that the DB state is visible in tunneling spectra at both sites is related to the $\simeq$1-nm lateral size of the DB wave function (see Supplemental Material, Fig. S5 [24]). The individual $\Delta f(V)$ spectroscopies are represented in Fig. 4(c). Colored data points indicate the [−0.4 V; 0.4 V] voltage range used to establish the quadratic fit. The difference between the $\Delta f(V)$ spectroscopies and the extrapolated parabolic fits is represented in Fig. 4(d) in the [−1 V; +1 V] voltage range.

V. DISCUSSION

The previous analysis enables us first to rule out any spurious relationship between $I_t(V)$ and $\Delta f(V)$ such as phantom forces [26] or quartz cross-talk effects [27]. In particular, no asymmetry is observed for positive and negative voltages for $\Delta f(V)$ on the p-type semiconductor substrate, while the $I_t(V)$ is highly asymetric. The absence of deviations for $\Delta f(V)$ when I_t is significant is further demonstrated in Fig. 4(d), in which the low-voltage fit to $\Delta f(V)$ (with $I_t < 10$ pA) perfectly applies in the full [−1 V; 1 V] range (with I_t up to 1 nA). Since the average current passed through the DB does not exceed the nanoampere range, this rules out any phantom force effect in the forthcoming analysis.

The analysis done in Fig. 4(d) enables us to further understand DB charging effects. They appear on the charging ring [red curve in Fig. 4(d)] as a linear increase in $\Delta f(V)$ for $V > 0.5$ V, with a slope of about 0.065 Hz/V, while only faint deviations with respect to a pure parabolic behavior are observed at the DB site itself [blue curve in Fig. 4(d)]. Averaged data are also available in Supplemental Fig. S4 [24]. The linear behavior is equivalent to a constant surface potential offset δV_s, inducing a linear frequency shift contribution $2B\delta V_s \times V$.

This shows, in particular, that the charging does not vary with the sample voltage. Using $B = 0.13$ V/Hz^2 as from the fit in Fig. 4(c), this yields $\delta V_s = 250$ mV (with a misaccuracy of 10%). The linear fit of $\Delta f(V)$ for $V > 0.5$ V also evidences a frequency shift jump at $V \approx 0.5$ V, of amplitude 15 ± 7 mHz, however close to the experimental noise. We attribute the δV_s value to the transition between the DB^+ charge state and the DB^0 charge state. It is, in particular, consistent with a dark-to-bright transition in the KPFM image, since the DB^+ charge state electrostatic potential is of ≈ -80 mV (see Supplemental Material, Fig. S2 [24]).

A phenomenological model explaining the ring-shape transition from the DB^+ to the DB^0 charge state is finally proposed in Fig. 4(e). It is based on the shape of the DB wave function, with a lateral extension of about 1 nm on the AFM/STM tip side and a reduced extension on the substrate side. The carrier injection into the DB wave function is governed by the wave-function overlaps between the DB and the tip outermost atom, while the recombination between an electron populating the DB and a substrate hole is more local. The latter process has been treated so far as in bulk semiconductors, with a rate described as $c \times p$ in which c is the hole capture coefficient [16]. We propose that tip charging and/or polarization effects can induce the appearance of the charging ring, via the modulation of the hole capture rate $c \times p$. Assuming here for discussion a charge picture in which the grounded tip carries a local charge δ^- with a corresponding substrate image δ^+, for $V > 0$ (this charge may be replaced by a short-range polarization effect), this local charge follows the outermost tip atom when the tip is scanned over the DB [Fig. 4(e)]. This enhances the recombination rate $c \times p$ (and thus lowers the average DB electron occupancy) when the tip is above the DB Si adatom. The recombination rate is conversely lower when the tip is positioned at the edge of the wave function. Altogether, this leads to an enhanced DB charging effect, with a ring shape corresponding to the DB wave-function diameter. δ^+ can be estimated using the capacitance $4\pi\epsilon_0 R$ of a sphere with radius $R = 1.7$ Å in order to mimic an outermost Si tip adatom, yielding $\delta^+ \approx 0.05e$ for $V = 0.5$ V. Even if δ^+ were "diluted"over a 1-nm^3 volume below the semiconductor surface, one gets $\delta p \approx$ a few 10^{16} cm^{-3}, which falls above the hole density p at the sample surface. This underlines the efficiency of a tip-induced modulation of $c \times p$ to explain the DB ring charging. A realistic model, however, clearly lies beyond our work since it will require the exact electronic structure of the Si(111)-$(\sqrt{3} \times \sqrt{3})R^\circ 30$ surface and the calculation of electrostatic short-range effects, including dipolar [28] and polarization [29] effects, which have been pointed out in the nc-AFM imaging of charged adatoms [2].

VI. CONCLUSION

In conclusion, we have achieved subnanometer electrostatic mapping of semiconductor defects carrying elementary charges and studied the charging mechanisms of a single Si DB. Remarkably, KPFM spectroscopy revealed nonparabolic features identified as a transition from the inoccupied DB^+ state to the single-occupied DB^0 state, with a ring shape localized at the edge of the DB wave function, and attributed to a modulation of the DB hole capture rate at the nanometer scale.

ACKNOWLEDGMENTS

We acknowledge discussions with M. Berthe and C. Delerue. This work was achieved using the facilities of the EXCELSIOR Nanoscience Characterization Center and of the RENATECH program.

[1] L. Gross, F. Mohn, N. Moll, P. Liljeroth, and G. Meyer, The chemical structure of a molecule resolved by atomic force microscopy, Science **325**, 1110 (2009).

[2] L. Gross, F. Mohn, P. Liljeroth, J. Repp, F. J. Giessibl, and G. Meyer, Measuring the charge state of an adatom with noncontact atomic force microscopy, Science **324**, 1428 (2009).

[3] W. Steurer, J. Repp, L. Gross, I. Scivetti, M. Persson, and G. Meyer, Manipulation of the Charge State of Single Au Atoms on Insulating Multilayer Films, Phys. Rev. Lett. **114**, 036801 (2015).

[4] F. Mohn, L. Gross, N. Moll, and G. Meyer, Imaging the charge distribution within a single molecule, Nat. Nanotechnol. **7**, 227 (2012).

[5] P. Hapala, M. Svec, O. Stetsovych, N. J. van der Heijden, M. Ondráček, J. van der Lit, P. Mutombo, I. Swart, and P. Jelinek, Mapping the electrostatic force field of single molecules from high-resolution scanning probe images, Nat. Commun. **7**, 11560 (2016).

[6] P. Jelinek, High resolution SPM imaging of organic molecules with functionalized tips, J. Phys.: Condens. Matter **29**, 343002 (2017).

[7] S. Sadewasser and T. Glatzel (Eds.), in *Kelvin Probe Force Microscopy From Since Charge Detection to Device Characterization* (Springer, New York, 2018).

[8] R. Stomp, Y. Miyahara, S. Schaer, Q. Sun, H. Guo, P. Grutter, S. Studenikin, P. Poole, and A. Sachrajda, Detection of Single-Electron Charging in an Individual InAs Quantum Dot by Noncontact Atomic-Force Microscopy, Phys. Rev. Lett. **94**, 056802 (2005).

[9] Y. Azuma, M. Kanehara, T. Teranishi, and Y. Majima, Single Electron on a Nanodot in a Double-Barrier Tunneling Structure Observed by Noncontact Atomic-Force Spectroscopy, Phys. Rev. Lett. **96**, 016108 (2006).

[10] T. H. Nguyen, G. Mahieu, M. Berthe, B. Grandidier, C. Delerue, D. Stiévenard, and P. Ebert, Coulomb Energy Determination of a Single Si Dangling Bond, Phys. Rev. Lett. **105**, 226404 (2010).

[11] H. Labidi, M. Taucer, M. Rashidi, M. Koleini, L. Livadaru, J. Pitters, M. Cloutier, M. Salomons, and R. A. Wolkow, Scanning tunneling spectroscopy reveals a silicon dangling bond charge state transition, New J. Phys. **17**, 073023 (2015).

[12] T. Huff, H. Labidi, M. Rashidi, L. Livadaru, T. Dienel, R. Achal, W. Vine, J. Pitters, and R. A. Wolkow, Binary atomic silicon logic, Nat. Electron. **1**, 636 (2018).

[13] D. Eom, C.-Y. Moon, and J.-Y. Koo, Switching the charge state of individual surface atoms at Si(111)$\sqrt{3} \times \sqrt{3}$:B surfaces, Nano Lett. **15**, 398 (2015).

[14] R. Achal, M. Rashidi, J. Croshaw, T. R. Huff, and R. A. Wolkow, Detecting and directing single molecule binding events on H-Si (100) with application to ultradense data storage, ACS Nano **14**, 2947 (2020).

[15] M. Berthe, A. Urbieta, L. Perdigao, B. Grandidier, D. Deresmes, C. Delerue, D. Stiévenard, R. Rurali, N. Lorente, L. Magaud, and P. Ordejon, Electron Transport via Local Polarons at Interface Atoms, Phys. Rev. Lett. **97**, 206801 (2006).

[16] M. Berthe, R. Stiufiuc, B. Grandidier, D. Deresmes, C. Delerue, and D. Stiévenard, Probing the carrier capture rate of a single quantum level, Science **319**, 436 (2008).

[17] M. Taucer, L. Livadaru, P. G. Piva, R. Achal, H. Labidi, J. L. Pitters, and R. A. Wolkow, Single-Electron Dynamics of an Atomic Silicon Quantum Dot on the H-Si (100) - 2 $\times$ 1 Surface, Phys. Rev. Lett. **112**, 256801 (2014).

[18] M. Rashidi, M. Taucer, I. Ozfidan, E. Lloyd, M. Koleini, H. Labidi, J. L. Pitters, J. Maciejko, and R. A. Wolkow, Time-Resolved Imaging of Negative Differential Resistance on the Atomic Scale, Phys. Rev. Lett. **117**, 276805 (2016).

[19] K. Teichmann, M. Wenderoth, S. Loth, R. G. Ulbrich, J. K. Garleff, A. P. Wijnheijmer, and P. M. Koenraad, Controlled charge Switching on a Single Donor with a Scanning Tunneling Microscope, Phys. Rev. Lett. **101**, 076103 (2008).

[20] E. J. Spadafora, J. Berger, P. Mutombo, M. Telychko, M. Svec, Z. Majzik, A. B. McLean, and P. Jelínek, Identification of surface defects and subsurface dopants in a delta-doped system using simultaneous nc-AFM/STM and DFT, J. Phys. Chem. C **118**, 15744 (2014).

[21] S. Torbrügge, O. Schaff, and J. Rychen, Application of the Kolibrisensor to combined atomic-resolution scanning tunneling microscopy and noncontact atomic-force microscopy imaging, J. Vac. Sci. Technol. **28**, C4E12 (2010).

[22] Y. Sugimoto and J. Onoda, Force spectroscopy using a quartz length extension resonator, Appl. Phys. Lett. **115**, 173104 (2019).

[23] J. Berger, E. Spadafora, P. Mutombo, P. Jelínek, and M. Švec, Force-driven single-atom manipulation on a low-reactive Si surface for tip sharpening, Small **11**, 3686 (2015).

[24] See Supplemental Material at http://link.aps.org/supplemental/10.1103/PhysRevB.102.235433 for additional data about KPFM experiments performed on a single surface silicon vacancy; comparative KPFM results on a single buried dopant, silicon vacancy, and Si dangling bond; the electrostatic structure and expected KPFM signals for the neutral dangling bond (DB^0 state) and the positively charged dangling bond (DB^+ state); averaged $\Delta f(V)$ spectroscopy on the dangling bond charging ring; and simultaneous KPFM and tunnel spectroscopy data on the dangling bond.

[25] F. J. Giessibl, F. Pielmeier, T. Eguchi, T. An, and Y. Hasegawa, Comparison of force sensors for atomic force microscopy based on quartz tuning forks and length-extensional resonators, Phys. Rev. B **84**, 125409 (2011).

[26] A. J. Weymouth, T. Wutscher, J. Welker, T. Hofmann, and F. J. Giessibl, Phantom Force Induced by Tunneling Current: A Characterization on Si(111), Phys. Rev. Lett. **106**, 226801 (2011).

[27] L. Nony, F. Bocquet, F. Para, and C. Loppacher, Frequency shift, damping, and tunneling current coupling with quartz tuning forks in noncontact atomic force microscopy, Phys. Rev. B **94**, 115421 (2016).

[28] T. Mélin, H. Diesinger, D. Deresmes, and D. Stiévenard, Probing Nanoscale Dipole-Dipole Interactions by Electric Force Microscopy, Phys. Rev. Lett. **92**, 166101 (2004).

[29] F. Bocquet, L. Nony, and C. Loppacher, Polarization effects in noncontact atomic force microscopy: A key to model the tip-sample interaction above charged adatoms, Phys. Rev. B **83**, 035411 (2011).